Controlled Synthesis of Hierarchical CuO Nanostructures for Electrochemical Capacitor Electrodes

Yu Xin Zhang[1,2,], Ming Huang[1], Fei Li[1], Zhong Quan Wen[2]*

[1]College of Material Science and Engineering, Chongqing University, Chongqing, 400044, P.R. China
[2]Key Laboratory of Fundamental Science of Micro/Nano-Devices and System Technology, Chongqing University, Chongqing, 400044, P.R. China
[*]E-mail: zhangyuxin@cqu.edu.cn

Nanostructured CuO with diverse morphologies has been synthesized via a facile and scaleable wet-chemical method, accompanied with calcination. As-prepared CuO nanostructures were characterized using x-ray diffraction spectroscopy (XRD), fourier transform infrared spectroscopy (FTIR), focus ion beam scanning electron microscopy (FIB/SEM), transmission electron microscopy (TEM) and nitrogen adsorption-desorption. The electrochemical properties of the CuO electrodes were elucidated by cyclic voltammograms, galvanostatic charge-discharge tests and electrochemical impedance spectroscopy in aqueous 6 M KOH electrolyte. The electrochemical results demonstrated that the specific capacitance of the nanostructured CuO strongly depended on their morphologies (nanosheets-like, bundle-like and flower-like CuO). Remarkably, the as-synthesized CuO nanosheets exhibited a higher specific capacitance of 88.5 F g^{-1} at the scan rate of 2 mV s^{-1}. The capacitance retention of CuO nanosheets was around 90.6 % after 500 charge/discharge cycles at a current density of 5 mA cm^{-2}. In principles, these findings suggested that the low-cost CuO nanostructures could be a promising candidate for electrochemical capacitor electrode material.

1. INTRODUCTION

Electrochemical capacitors also known as supercapacitors, are electrochemical energy storage devices used as intermediates between conventional dielectric capacitors and batteries [1-3]. In recent years, supercapacitors have attracted significant research attention as efficient energy storage devices due to their properties like high power density, excellent reversibility and long cycle life for time-dependent power needs of modern electronics and power systems [4-7]. Based on the charge storage

mechanisms, they can be divided into two categories, namely, electric double layer capacitors (EDLCs) and pseudocapacitors [8, 9]. The capacitance of the former comes from the charge accumulation at the electrode/electrolyte interface, and the latter's capacitance is due to the fast reversible faradaic transitions of electro-active species of the electrode. To date, carbon-related materials have been widely utilized as building blocks to construct electrodes for EDLCs due to their good processing ability, large surface area/porosity, good cycle life, and low cost [10-12], but the devices fabricated suffer from their relative low capacity in storing charge. In contrast, the electrochemical capacitors can afford a higher energy storage capacity [13-15]. Transition metal oxides are considered as ideal electrode materials for pseudocapacitors as they can provide a variety of oxidation states for efficient redox charge transfer. RuO_2 and IrO_2 of noble metal oxide materials were used as pseudocapacitive electrode materials with remarkable performance [16-19], however, the high cost of hydrous ruthenium oxide and iridium oxide hindered their wide application. Hence, more efforts have been aimed at searching for cheap electrode materials including Fe_2O_3 [20], MnO_2 [21, 22], NiO [23, 24], Co_3O_4 [25], and CuO [26] for exploring alternative pathways to tailor the functionalities of electrode materials and construct supercapacitors with enhanced energy and power densities.

As an important p-type transition-metal oxide with a narrow band gap (E_g=1.2 eV), CuO has been explored as an electrode material for high-power electrochemical pseudocapacitors due to its abundant resources, environmental compatibility, cost effectiveness and favorable pseudocapacitive characteristics. It was found that the morphology and particle size of CuO remarkably affected its specific capacity. For instance, Patake et al. [27, 28] synthesized the porous amorphous copper oxide thin films which exhibited a specific capacitance around 40 F g^{-1} in 1 M Na_2SO_4 electrolyte. Zhang et al. [29, 30] showed that CuO with flower-like nanostructures displayed a higher specific capacitance of 133.6 F g^{-1} in 6 M KOH electrolyte, which is about three-fold higher than commercial CuO powder. Li et al. [31] found that the CuO nanosheets directly grown onto copper foam exhibited a specific capacitance as high as to 212 F g^{-1} at a current density of 0.41 mA mg^{-1} in 6.0 M KOH electrolyte. Wang et al. [32] have reported the synthesis of CuO nanosheet arrays directly grown onto nickel foam with higher specific capacitance of 569 F g^{-1}. As inspired by its novel properties and great potential applications, nano-sized CuO nanostructures with diverse morphologies have been synthesized via a variety of methods [33-38]. However, the synthetic procedures for these unique morphology materials are still relatively complicated and low yield. Thus, the controlled synthesis of CuO nanostructures with enhanced supercapacitor performance still requires easy operation, low cost, and high yield, which are favorable from the viewpoint of practical application. To the best of our knowledge, there were few reports explored the controlled synthesis of CuO nanostructures with diverse morphologies and investigated the electrochemical performance simultaneously.

In this study, we have prepared porous CuO nanostructures with different morphologies under a controlled method in the presence of tetraoctylammonium bromide (TOAB) at room temperature. The morphology, structure and electrochemical properties of the CuO nanostructures were investigated and the correlation between the morphology and electrochemical performance was examined.

2. EXPERIMENTAL

2.1 Materials

Copper nitrate ($Cu(NO_3)_2 \cdot 3H_2O$), sodium hydrate (NaOH), potassium hydrate (KOH), ammonia ($NH_3 \cdot H_2O$), ethanol (C_2H_5OH), tetraoctylammonium bromide (TOAB), polyvinylidene fluoride (PVDF) and solvents used in this work were purchased from Alfa Aesar. The entire chemicals were of analytical purity and used without any further purification.

2.2 Synthesis of porous CuO nanostructures with diverse morphologies

The CuO nanostructures were prepared with surfactant-assisted wet-chemical method followed by thermal treatment. Typically, an aqueous solution of $Cu(NO_3)_2 \cdot 3H_2O$ (20 mL, 0.05 M) was mixed with TOAB ethanol solution (40 mL, 0.05 M) in a round-bottom flask at room temperature and kept vigorous stirring for 5 min. Afterwards, different amount (2 mL, 4 mL, 6 mL, 8 mL) of $NH_3 \cdot H_2O$ (25-28%) was injected quickly. And then aqueous NaOH solution (10 mL, 1.00 M) was dropwisely added into the mixture and the mixture was kept vigorous stirring for 1.5 h. The resulting dark blue precipitates were separated, centrifuged, washed with distilled water and ethanol for several times, and dried at 60 °C in vacuum, giving the intermediate products. Finally, the intermediate products were calcined at 500 °C in air for 1 h.

2.3 Characterization

The crystallographic information and chemical composition of as-prepared products were established by powder X-ray diffraction (XRD, D/max 1200, Cu Kα) , fourier transform infrared spectroscopy (FTIR, Nicolet 5DXC), and thermogravimetric analyzer-differential scanning calorimeter (TGA-DSC, NETZSCH STA 449C). The structural and morphological investigations of the CuO nanostructures were carried out with high-resolution transmission electron microscopy (HRTEM, ZEISS LIBRA 200), field emission scanning electron microscopy (FESEM, FEI NOVA 400) and focused ion beam (ZEISS AURIGA FIB/SEM). Nitrogen adsorption-desorption isotherms were measured at 77K with micrometritics ASAP 2020 sorptometer. The specific surface area was calculated with the Brunauer-Emmett-Teller (BET) equation, and the pore size distributions were calculated from the adsorption curve by the Barrett–Joyner–Halenda (BJH) method.

2.4 Electrochemical measurements

The electrochemical measurements including cyclic voltammetry (CV), galvanostatic charge-discharge (GC) and electrochemical impedance spectroscopy (EIS) tests were performed by using a CHI 660E electrochemical workstation under ambient conditions. In a typical electrochemical measurement, a three-electrode cell system was composed of CuO powders electrode as the working electrode, a platinum plate as the counter electrode, and a saturated calomel electrode as the reference

electrode. The working electrode was fabricated by mixing the 70 wt% as-prepared CuO with 20 wt% carbon black (Super P) and 10 wt% polyvinylidene fluoride (PVDF), and then a slurry of above mixture was painted onto the foamed nickel as a current collector. The coated mesh was dried at 120 ^{o}C in vacuum cabinet overnight to remove the solvent and water.

The capacitive behaviors of the CuO nanostructures were characterized by cyclic voltammetry (CV) in 6 M KOH electrolyte at room temperature. CV measurements were performed on the three-electrode cells in the voltage window between 0 and 0.4 V at different scan rates. Galvanostatic charge-discharge experiments were performed with different current densities to reflect the rate ability. EIS measurements were carried out by applying an AC voltage with 5 mV amplitude in a frequency range from 0.01 Hz to 100 kHz at the open potential.

3. RESULTS AND DISCUSSION

3.1 Structure and morphology

Fig. 1 presents the composition and crystallite phase purity of the as-prepared $Cu(OH)_2$ precursor nanostructures. Diffraction peaks were observed of 16.6 ^{o}, 23.8 ^{o}, 34.1 ^{o}, 39.8 ^{o} and 53.2 ^{o}, and could be assigned to the (020), (021), (002), (130) and (150) planes of orthorhombic $Cu(OH)_2$ (JCPDS card no. 13-0420, a = 2.949 Å, b = 10.59 Å, c =5.256 Å), which confirmed a high degree of crystallinity, similar to the previous literature [39].
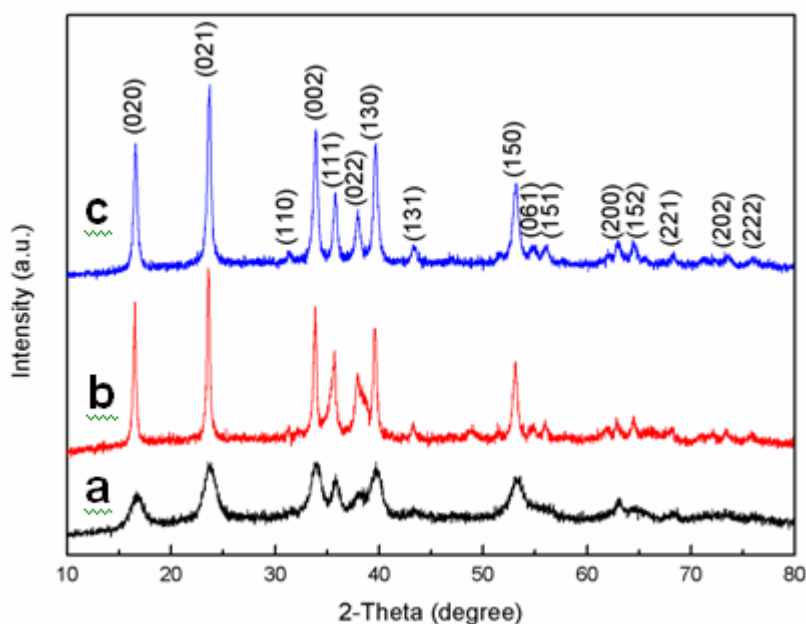

Figure 1. XRD patterns of different $Cu(OH)_2$ nanocrystallines obtained in presence of TOAB, $NH_3 \cdot H_2O$ and NaOH at room temperature for varied amount of $NH_3 \cdot H_2O$: a) 2 mL; b) 4 mL; c) 8 mL.

And the XRD patterns of the sample prepared with 6 mL of $NH_3 \cdot H_2O$ is the same as the above (See Supplementary Information, SI-1). The dominant peaks located at 2θ values between 10° and 80° clearly indicated that the intermediate $Cu(OH)_2$ product was a pure phase, while no characteristic peaks of impurities such as CuO and Cu_2O were detected.

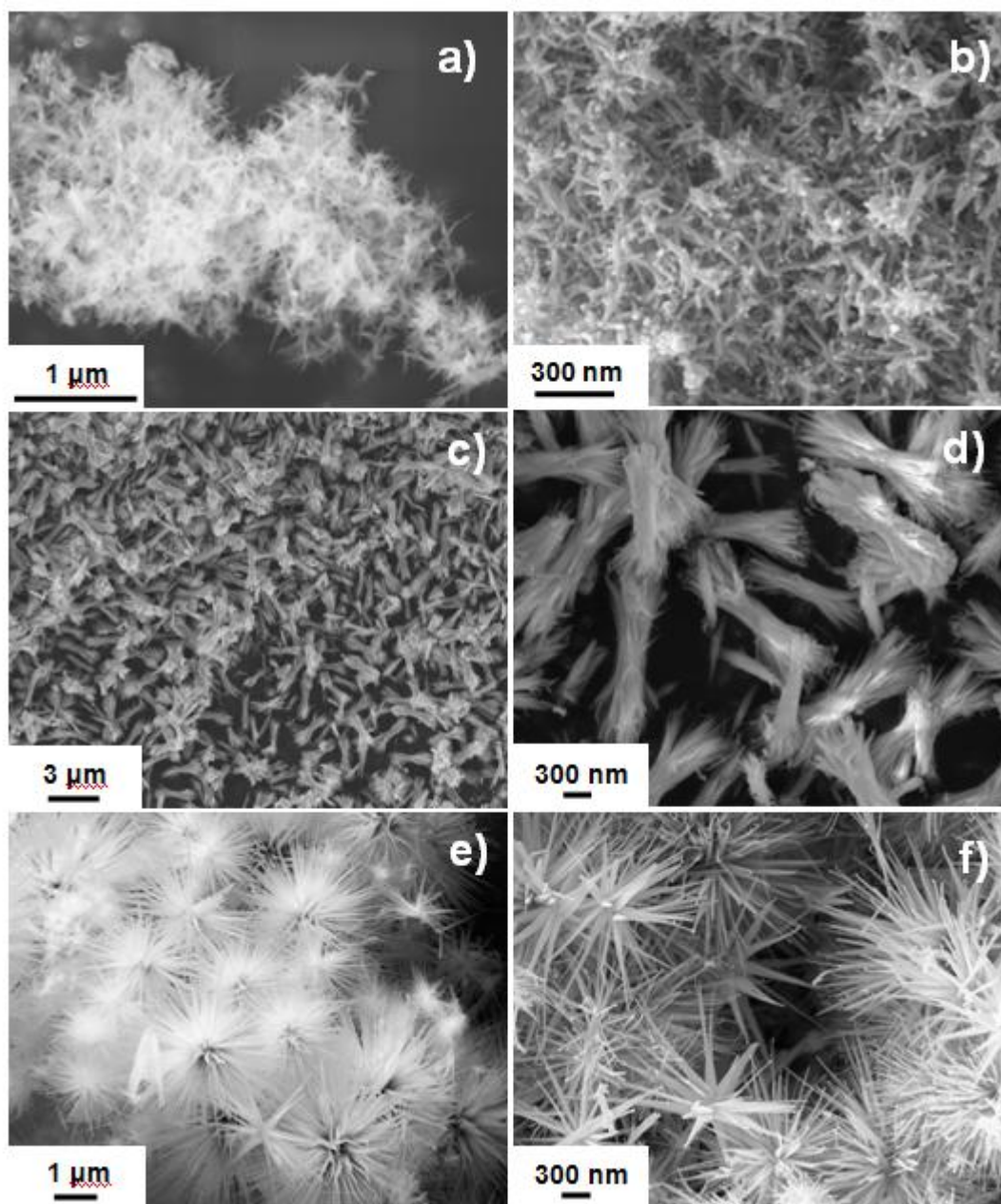**Figure 2.** Morphology of mesoporous $Cu(OH)_2$ precursor nanocrystallines obtained in presence of TOAB, $NH_3 \cdot H_2O$ and NaOH at room temperature for varied amount of $NH_3 \cdot H_2O$ with different magnification: a, b) 2 mL; c, d) 4 mL; e ,f) 8 mL.

The morphologies of the as-prepared $Cu(OH)_2$ nanostructures are presented with SEM images in Fig. 2. Fig. 2a and b show the $Cu(OH)_2$ nanostructures synthesized in the presence of $NH_3 \cdot H_2O$ (2 mL). It revealed that the as-prepared $Cu(OH)_2$ precursor had a sheet-like structure of 300 nm in length

and 60 nm in width. When the amount of $NH_3 \cdot H_2O$ was 4 mL, bundle-like CuO was obtained. Fig. 2c and d showed that the bundle-like CuO was self-assembled by small nanosheets. Observations at high magnification in Fig. 2d revealed that the width and length of the bundle-like CuO were about 600 nm and 4 μm, respectively. As the amount of $NH_3 \cdot H_2O$ was 6 mL, some incomplete flower-like could be obtained (See Supplementary Information, SI-2). Remarkably, when the addition of $NH_3 \cdot H_2O$ was 8 mL, we found that the $Cu(OH)_2$ exhibited a uniform flower-like structure of 3-5 μm in diameter. As shown in Fig. 2e and f, the flower-like CuO were also self-assembled by some small nanosheets (100 nm in width, 1-2 μm in length). These results indicated that the dosage of ammonia would greatly affect the morphology, aggregation, size and shape of the building blocks, which was due to the fact that the concentration of $NH_3 \cdot H_2O$ was considered to significantly affect the nucleation and growth behaviors (such as the number of nuclei and the concentration of growth units) of the nanocrystals.
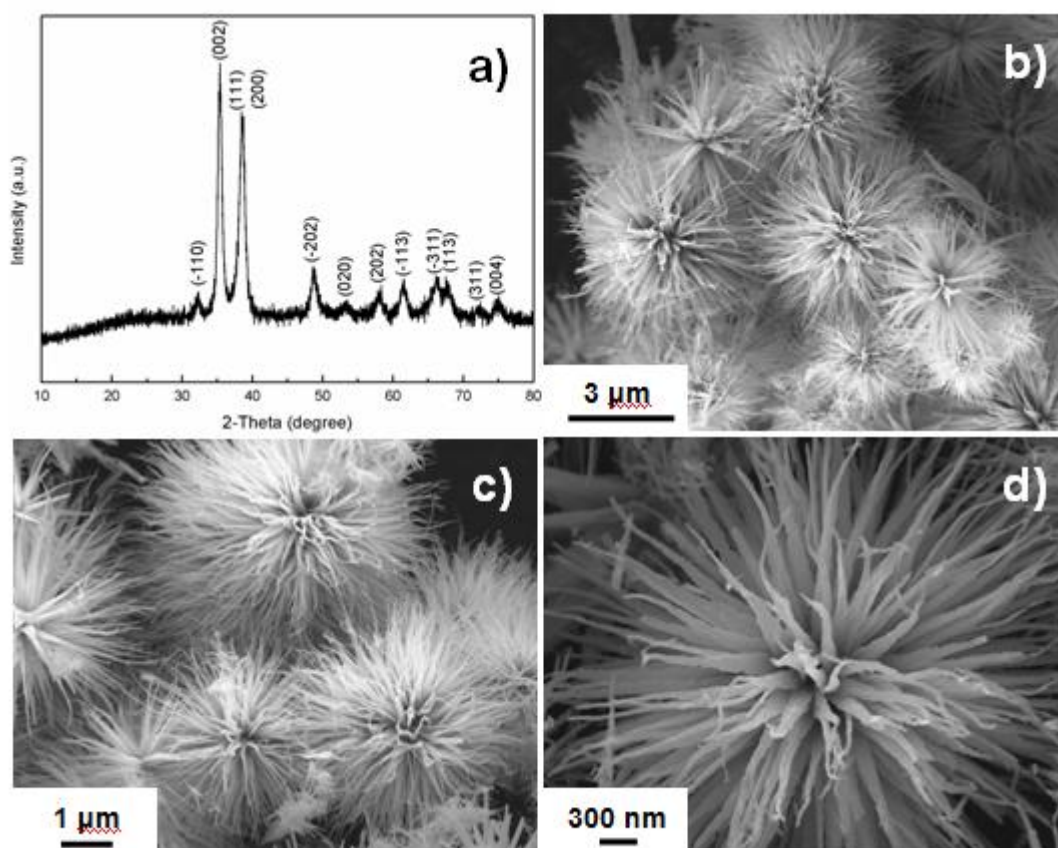

Figure 3. (a) XRD pattern of flower-like CuO gained by annealing $Cu(OH)_2$ precursor (Fig. 2e, f) at 500 ^{o}C for 1h; (b, c) detailed SEM images of the as-prepared flower-like CuO nanostructures; (d) a detailed view on an individual flower-like CuO . Note that the $Cu(OH)_2$ precursor was obtained with 8 mL $NH_3 \cdot H_2O$ in presence of TOAB and NaOH at room temperature with continuous stirring for 1.5 h.

Fig. 3 shows the structure of the flower-like CuO was further investigated by annealing $Cu(OH)_2$ precursor at 500 ^{o}C for 1 h. As shown in Fig. 3a, the XRD pattern shows the appearance of

reflections attributed to the monoclinic CuO (JCPDS card no. 45-0937, *a* = 4.685 Å, *b* = 3.426 Å, *c* =5.13 Å and *β* = 99.55°), similar to the previous reports [39]. Except for these CuO peaks, no other peaks were observed, indicating the high purity of as-obtained CuO products. Fig.3b and c show the detailed images of the as-prepared flower-like CuO nanostructures, which again indicated that the flower-like structure was composed of small nanoplates. The high magnification image on an individual flower-like CuO nanostructure is shown in Fig. 3d. The unique feature of this morphology was that each nanosheet in the flower-like structure would have its own electrical contact with the current collector, which may result in better charge transfer kinetics, leading to an enhancive electrochemical capacity.
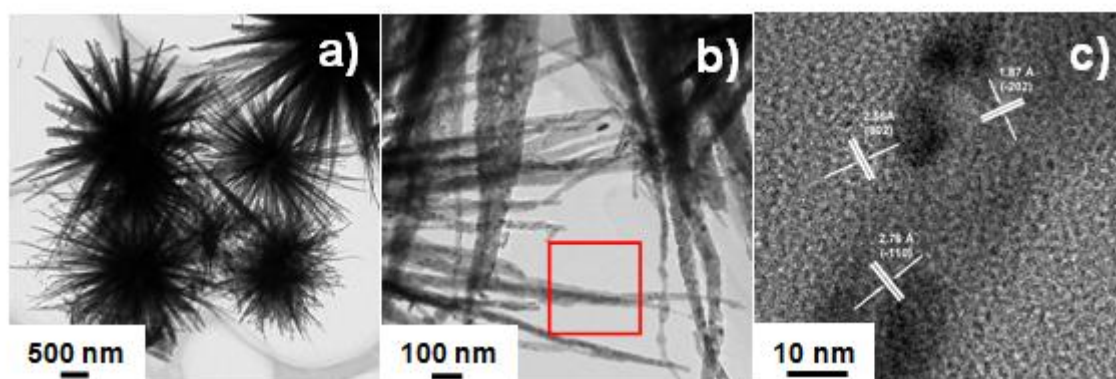

Figure 4. (a, b) TEM images of the as-prepared flower-like CuO (Fig. 3) gained by annealing $Cu(OH)_2$ precursor (Fig. 2e, f) at 500 °C for 1h; (c) HRTEM images (the boxed region in (b)) of the terminal part of the individual CuO nanosheet. Note that the $Cu(OH)_2$ precursor was obtained with 8 mL $NH_3 \cdot H_2O$ in presence of TOAB and NaOH at room temperature with continuous stirring for 1.5 h.

Fig. 4 presents transmission electron micrographs of the as-prepared flower-like CuO nanostructures (more TEM images were shown in Supplementary Information, SI-3). Detailedly, it can be observed that the flower-like CuO structures were uniform and monodispersed in Fig. 4a. Meanwhile, a higher magnification TEM image of the terminal part of the individual flower-like CuO was shown in Fig. 4b. Fig. 4c shows the HRTEM image of the boxed region in Fig. 4b. It shows the terminal part of the individual CuO nanosheet with the clear lattice fringes, as an indicative of the high crystallinity of the nanostructure skeleton. The interplanar distance of 2.76 Å can be ascribed to the (-110) plane of monoclinic CuO, while the interplanar distance of 2.56 Å and 1.87 Å can be ascribed to the (002) and (-202) plane, which was well consistent with the XRD results.

On the basis of the above experimental results, the plausible formation mechanism of CuO nanostructures was proposed. TOAB and $NH_3 \cdot H_2O$ were added to the aqueous solution of Cu^{2+} ions sequentially, forming a homogeneous deep blue $[Cu(NH_3)_n]^{2+}$ solution, where TOAB molecules were homogeneously dispersed. Upon adding aqueous NaOH solution, OH^- replaced NH_3 in the $[Cu(NH_3)_n]^{2+}$ complex to form square-planar $[Cu(OH)_4]^{2-}$ units, resulting in the formation of orthorhombic $Cu(OH)_2$ nanosheets [40]. Clearly, due to the different addition of $NH_3 \cdot H_2O$, separate

$Cu(OH)_2$ nanoplates formed and eventually self-assembled to give the varied $Cu(OH)_2$ nanostructures, and the similar morphology of CuO nanostructures could be obtained by thermal dehydration of the as-prepared $Cu(OH)_2$ precursors. Our previous work has demonstrated that the TOAB may act as a growth-directing agent which could modulate the kinetic growth [41].
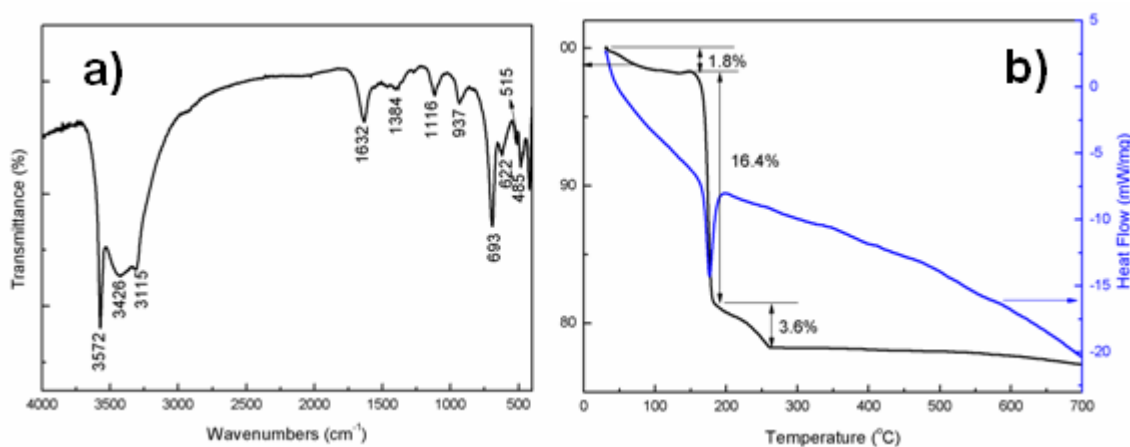
3.2 FT-IR and thermal properties

Figure 5. FT-IR spectra (a) and TGA-DSC curve (b) of the as-prepared $Cu(OH)_2$ precursor obtained with 8 mL $NH_3 \cdot H_2O$ in presence of TOAB and NaOH at room temperature with continuous stirring for 1.5 h.

The FTIR spectrum was used to investigate the surface properties of the $Cu(OH)_2$ precursor nanostructures (Fig. 5). As shown in Fig. 5a, the absorption peaks in the infrared spectrum of $Cu(OH)_2$ at low frequencies below 700 cm^{-1} are due to Cu-O vibrations, while bands centered at 3572, 3315 cm^{-1} correspond to the hydroxyl ions [42, 43]. The broad band centered at 3426 and 1632 cm^{-1} were attributed to the O-H stretching and bending modes of water [44, 45]. The weak bands around 1384 cm^{-1} corresponded to the C-H vibration and the absorption peak at 1116 cm^{-1} can be assigned to C-O vibration coordinating to metal cations, indicating few surfactants absorbed on the surface of $Cu(OH)_2$ samples.

To further confirm the possible coordination of TOAB with $Cu(OH)_2$ nanostructures, the simultaneous DSC and TGA analysis of flower-like $Cu(OH)_2$ were performed from room temperature to 700 °C in air (Fig. 5b). The first weight loss of 1.8 % between 30 °C and 150 °C resulted from the removal of physically absorbed water and chemically bound water. The temperature range from 150 to 180 °C and this particular weight loss (16.4%) may be ascribed to the loss of the decomposition of $Cu(OH)_2$ to give CuO. The sharp endothermic DSC peak around 170 °C was consistent with the decomposition of $Cu(OH)_2$ in as-prepared products, this feature was in good agreement with the previous TGA results of $Cu(OH)_2$ [46]. Within temperature interval from 180 to 260 °C, this particular weight loss (3.6%) may be ascribed to the loss of the decomposition of few residual surfactants. Furthermore, the as-prepared $Cu(OH)_2$ nanosheets with 2 mL $NH_3 \cdot H_2O$ was also investigated, and its DSC and TGA results was presented in supplementary information (SI-4). As no significant weight

loss has been observed beyond 400 ^{o}C in the sample, this result indicated that 400 ^{o}C could be considered as an appropriate calcination temperature.

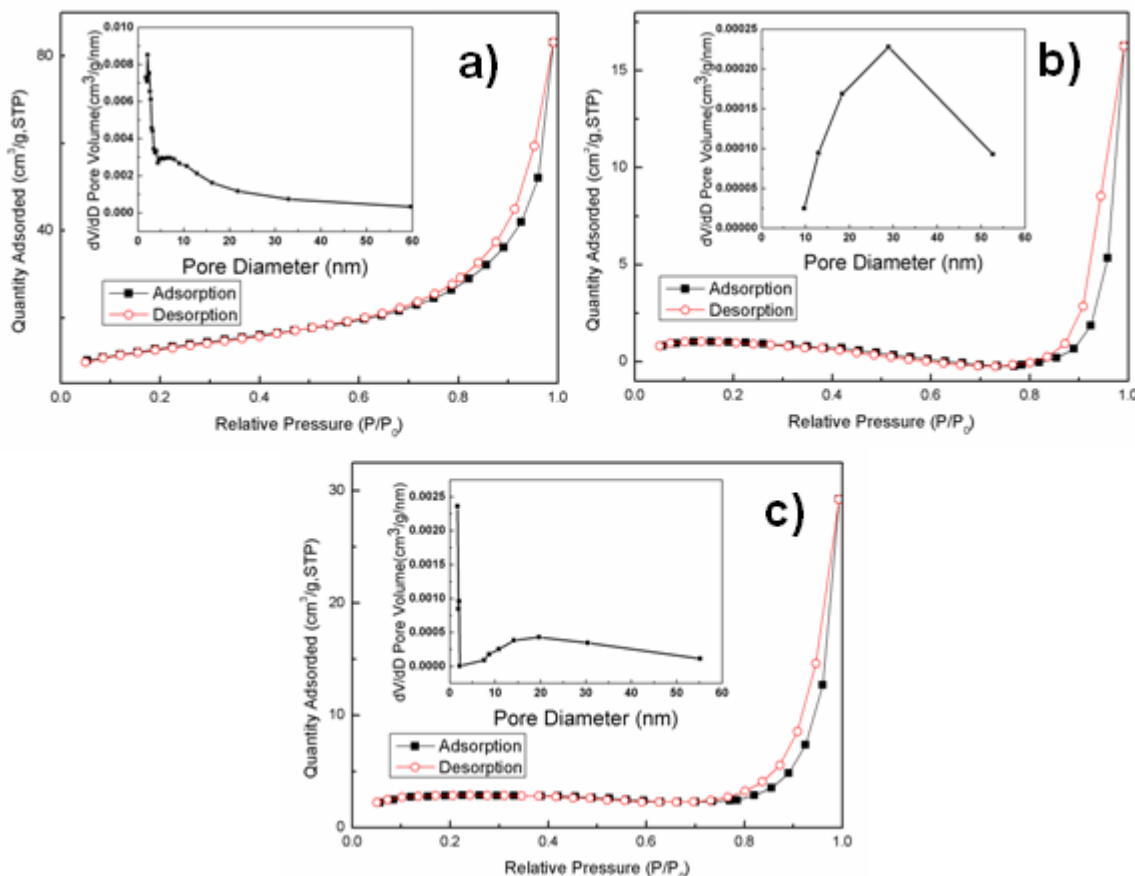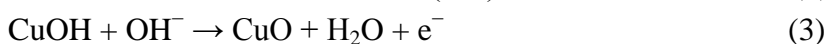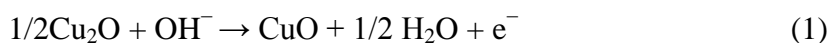*3.3. Surface area and porosity analysis*

Figure 6. N_2 adsorption-desorption isotherms and corresponding pore size distribution of the as-prepared CuO nanocrystallines obtained by annealing $Cu(OH)_2$ precursor at 500 ^{o}C for 1 h with different amount of $NH_3 \cdot H_2O$: a) 2 mL $NH_3 \cdot H_2O$; b) 4 mL $NH_3 \cdot H_2O$; c) 8 mL $NH_3 \cdot H_2O$.

To examine surface properties of the as-prepared varied CuO nanostructures, Brunnauer-Emmett-Teller (BET) and nitrogen adsorption-desorption measurement were performed. The corresponding nitrogen adsorption-desorption isotherm and pore size distribution curve (inset) of the CuO are shown in Fig. 6. The N_2 adsorption-desorption isotherm of the as-synthesized CuO nanostructures reflected a typical IV sorption behavior with the profile of a hysteresis loop in the high relative pressure (P/P$_0$) range between 0.7 and 1.0, indicating that the composite had a typical mesoporous structure. As shown in Fig. 6, the BET surface areas of the CuO nanosheet (obtained with 2 mL $NH_3 \cdot H_2O$ in Fig. 6a), bundle-like CuO (obtained with 4 mL $NH_3 \cdot H_2O$ in Fig. 6b), and flower-like CuO (obtained with 8 mL $NH_3 \cdot H_2O$ in Fig. 6c) are 45.1, 14.1, and 6.3 m^2 g^{-1}, respectively. From the Barrett-Joyner-Halenda (BJH) pore diameter distribution curve (inset in Fig. 6), the CuO

nanostructures exhibited the abundance of mesopores between 2 and 50 nm. And thus it can infer that the characteristic broad pore size distribution of the samples is an amalgamation of internal space of the agglomerated flakes, surface porosity of the flakes, and the porosity due to internal space of different morphology structures [47]. Such type of hierarchical surface morphologies with well developed pore structures were advantageous for enhancive electrochemical capacitors applications since large pore channels permitted rapid electrolyte transport, while the small pores provided more active sites for chemical reactions [48].

3.4 Electrochemical properties of the mesoporous CuO nanostructures

To evaluate the potential applications in electrochemical capacitors, the hierarchical porous CuO samples with different morphologies were used to make supercapacitor electrodes, and characterized with cyclic voltammetry, galvanostatic charge/discharge and impedance measurements in Fig. 7. As shown in Fig. 7a, c and e, CV curves of the CuO electrodes with different morphologies measured in a large scan rate range from 5 to 50 mV s^{-1} in the potential range 0-0.4 V vs. SCE. The CV profiles for all the three samples were very similar and quite different from the ideal rectangular shape for double layer capacitance, which suggested that the capacitance of CuO primarily originated from Faradic redox reactions. The different mass specific current densities indicated that the three samples had different specific capacitance. In the potential range of 0-0.4V, the following reactions between Cu(I) and Cu(II) species (Eqs.(1)-(4)) have been proposed [31, 49-53].

$$1/2Cu_2O + OH^- \rightarrow CuO + 1/2\ H_2O + e^- \tag{1}$$
$$1/2Cu_2O + 1/2H_2O + OH^- \rightarrow Cu(OH)_2 + e^- \tag{2}$$
$$CuOH + OH^- \rightarrow CuO + H_2O + e^- \tag{3}$$
$$CuOH + OH^- \rightarrow Cu(OH)_2 + e^- \tag{4}$$

The broad anodic peak can be attributed to the oxidation of Cu_2O and/or CuOH to both CuO and/or $Cu(OH)_2$. The broad cathodic peak can be ascribed to the reduction of CuO and/or $Cu(OH)_2$ to Cu_2O and/or CuOH. The broad peak feature could be results of the overlap of the redox peaks given in Eqs.(1)–(4). Clearly, it can be seen that the shapes of CV curves have no change and the redox-peak position is nearly consistent at different sweep rates, exhibiting stable electrochemical property and higher reversibility of the CuO nanostructures. In order to identify which architecture is favorable for high-rate capacitive energy storage, the specific capacitance values of the three samples have been determined by CV curves. The specific capacitance of the CuO electrode can be calculated from the CV curves according to the following equation

$$C_m = \frac{i}{mv} \tag{5}$$

where *m* is the mass of electroactive material CuO, *v* is the potential sweep rate, and *i* is the even current response defined by $i = \int_{V_a}^{V_c} i(V)dV/(V_c - V_a)$ (V_a and V_c represent the lowest and highest voltages, respectively) and obtained through integrating the area of the curves in Fig. 7a, c and e. The specific capacitance of CuO nanosheet, bundle-like CuO and flower-like CuO calculated from CV curves at the scan rate of 2 mV s^{-1} were 88.5, 49.2, and 68 F g^{-1}, respectively.
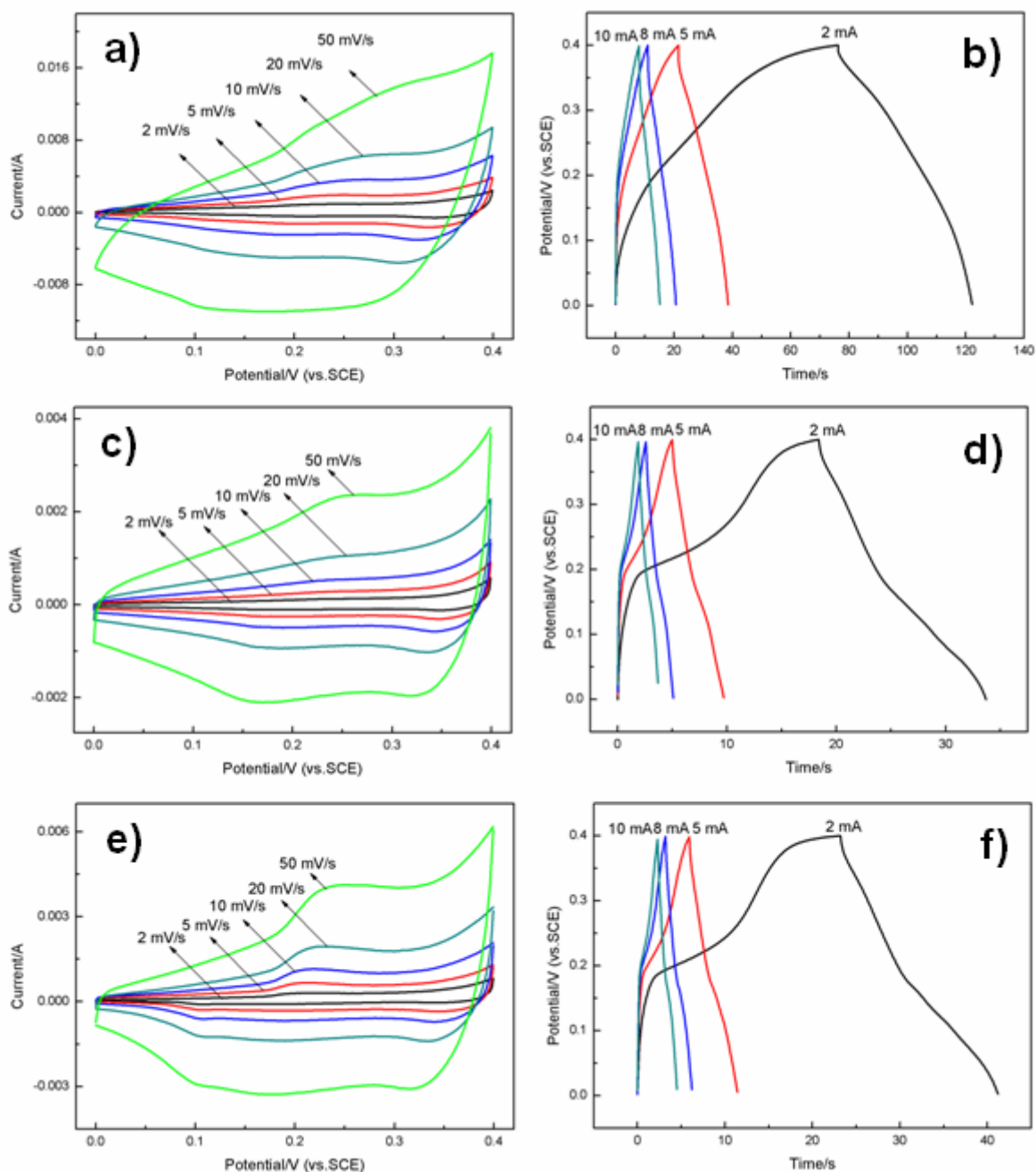
Figure 7. Cyclic voltammograms of CuO nanostructures with different morphologies at different scan rate (2, 5, 10, 20 and 50 mV s^{-1}) (a, c and e) in a 6 M KOH aqueous electrolyte; Corresponding charge-discharge curves of CuO electrodes (b, d and f) at different current densities (2, 5, 8 and 10 mA cm^{-2}). Note that the CuO nanocrystallines obtained by annealing Cu(OH)$_2$ precursor at 500 ^{o}C for 1 h with different amount of NH$_3$·H$_2$O : a, b) 2 mL NH$_3$·H$_2$O; c, d) 4 mL NH$_3$·H$_2$O; e, f) 8 mL NH$_3$·H$_2$O.

Additionally, galvanostatic constant current charge-discharge curves at various current densities were performed with an electrochemical window of 0-0.4 V to further examine the electrochemical performance of the CuO nanostructures with different morphologies. As shown in Fig. 7b, d, and f, the charge curves are almost linear and somewhat mirror symmetrical to their discharge

counterparts, suggestive of good electrochemical performance for the three mesoporous CuO samples. The specific capacitance of the mesoporous CuO can be calculated from the GC curves using the following equation

$$C_m = \frac{I \Delta t}{\Delta V m} \qquad (6)$$

where I, $\triangle t$, $\triangle V$, and m denote current density, discharge time, potential range in discharge after the IR drop, and the active weight of the electrode material, respectively. The specific capacitance values of the CuO nanosheets, bundle-like CuO and flower-like CuO electrodes at current density of 2 mA cm^{-2} were 85.7, 46.2, and 64.6 F g^{-1}, in good agreement with the CV results. According to the comparison of the specific capacitance among three CuO samples, it can be seen that CuO nanosheet electrode was higher than that of both bundle-like CuO and flower-like CuO. The bundle-like CuO exhibited the lowest specific capacitance, which was only about half of that of CuO nanosheets. This significant difference in the specific capacitance of CuO can be attributed to its difference in morphology. The morphology may affect the specific capacitance of CuO in three aspects: the electrical resistance, the electrolyte diffusion within CuO nanostructures and the specific surface area of CuO [29]. The bundle-like and flower-like CuO are longer and thus have larger electrical resistance than CuO nanosheet. Furthermore, the bundle-like and flower-like CuO structures were agglomerates of nanosheets and thus the electrolyte diffusion was more difficult than the individual nanosheet. The increasing order of the specific capacitance (bundle-like CuO < flower-like CuO < CuO nanosheet) was consistent with increasing sequence of CuO specific surface area, indicating that the highly mesoporous structure and high specific surface area of the electrode facilitates the ions to transfer into the porous structure more easily which would lead to more redox faradic reactions and surface adsorption of electrolyte cations.

Electrochemical impedance spectroscopy (EIS) has been applied at open circuit potential to investigate electrical conductivity and ion transfer of the supercapacitor test cell, and the Nyquist plots of the three CuO electrodes were shown in Fig. 8. The Nyquist plots for the three electrodes consisted of approximately a semicircle at high frequency and a linear region at low frequency. The equivalent circuit for the Nyquist plots is shown as an inset in Fig. 8. In this equivalent circuit, the symbols R_s, R_{ct}, C_d, and Z_w denoted the solution resistance, charge-transfer resistance, capacitance of the double layer, and Warburg impedance, respectively [54]. The intercept on real axis at high frequency reflected the equivalent series resistance (ESR), which was related to the electrolyte resistance, intrinsic electrical resistance of grains, and the contact resistances of grain-to-grain and grain-to-current collector [55]. The ESR values of CuO electrodes with nanosheet-like, bundle-like, and flower-like morphologies are 0.5, 0.95, and 0.65 Ω, respectively. The charge-transfer resistance (Rct) can be estimated from the diameters of semicircles on real axis. It can be seen that the charge-transfer resistance decreased in the order of bundle-like CuO > flower-like CuO > CuO nanosheet. This order was consistent with the decrease of specific capacitance of the three electrodes. The low frequency region consisted of two straight lines: the one with smaller slope can be ascribed to Warburg impedance related to the diffusion of electrolyte within the CuO structures; the one with larger slope demonstrated the capacitance nature of the electrode (vertical line for an ideal capacitor). All the above impedance results explained the best pseudocapacitor performance of the CuO nanosheet electrode.
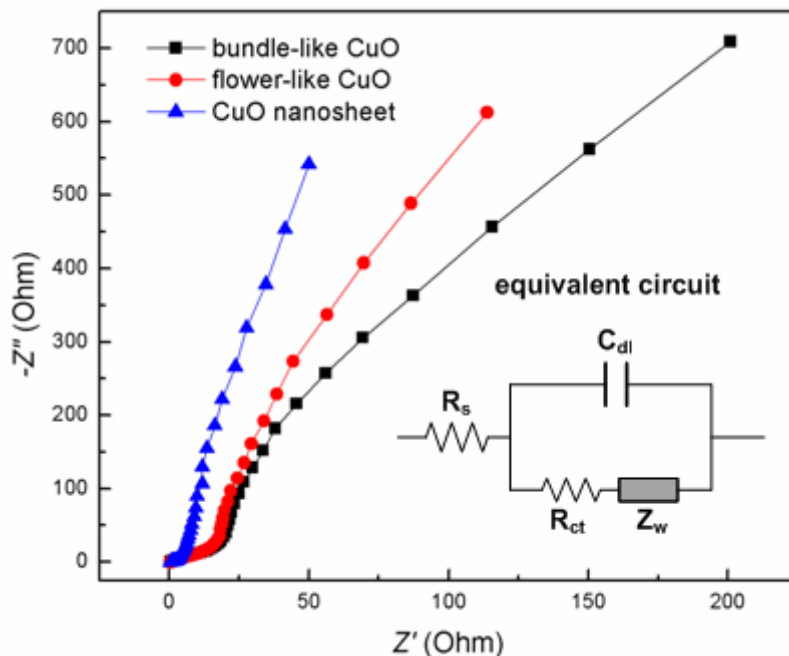
Figure 8. The electrochemical impedance spectrum of the CuO electrodes with different morphologies in 6.0 M KOH at open circuit potential in the frequency range from 0.01 Hz to 100 kHz.
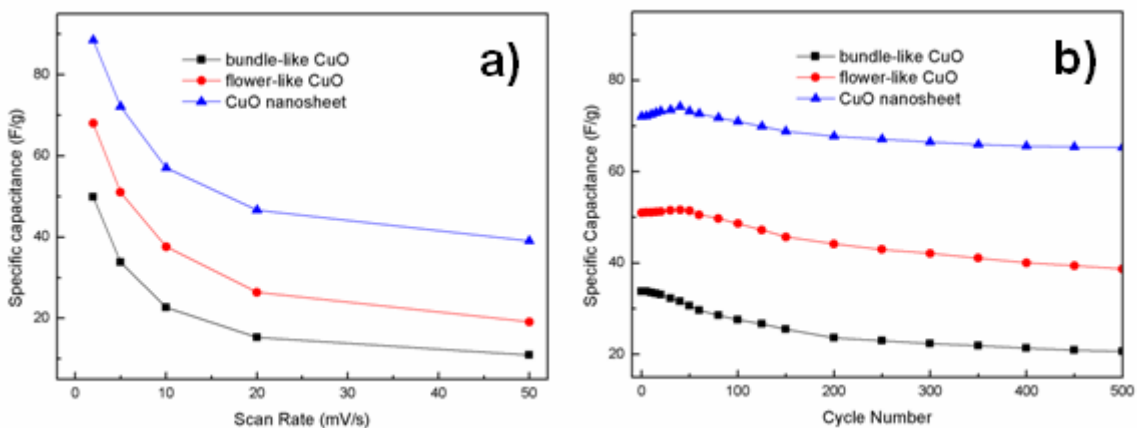

Figure 9. (a) Specific capacitance of CuO nanostructures measured under different scan rates; (b) cycling performance for different CuO electrodes at a current density of 5 mA cm^{-2} in 6 M KOH.

The dependence of the specific capacitance on the scan rates and the cycling performance of three samples are shown in Fig. 9. As shown in Fig. 9a, it can be seen that the capacitances of the CuO nanostructures decreased slightly with increasing scan rates from 2 to 50 mV cm^{-1}. The capacitance retentions were calculated to be 45.4 %, 28.1 %, and 23.0 % for CuO nanosheet, flower-like CuO, and bundle-like CuO, respectively. The decrease of the specific capacitance may be caused by the internal resistance of the electrode. At lower current densities, ions could penetrate into the inner-structure of electrode material, having access to almost all available pores of the electrode, but at higher current

densities, an effective utilization of the material was limited only to the outer surface of electrodes. The good rate capability of CuO nanosheet may be attributed to the unique mesoporous microstructures and its high specific surface area.

The working stability of energy storage devices was also crucial for their practical applications, and thus we further performed the charge-discharge cycling test to examine the cycling ability of the electrodes made with the CuO nanostructures. Fig. 9b indicates the long-term electrochemical stability of the synthesized CuO electrodes (bundle-like CuO, flower-like CuO, and CuO nanosheet) in 6 M KOH electrolyte by charge-discharge cycling at current density of 5 mA cm^{-2} for consecutive 500 cycles. A slight increase in the capacitances was observed during the first 50 cycles for the CuO nanosheet electrodes which was attributed to the activation process [56] allowing the trapped cations in the CuO crystal lattice to gradually diffuse out. Such increase in the capacitance during cycling test was not detectable for the flower-like CuO and bundle-like CuO. This was possibly due to the decrease in capacitance as the electrodes degraded during the cycling charge/discharge processes, which obscured the activation effect [57]. As can be seen that after 500 cycles, the electrodes made by CuO nanosheet, flower-like CuO, and bundle-like CuO can retain approximately 90.6, 76.0, and 63.5 % of their initial value processes, respectively. The excellent performances in cycling stability of the CuO nanosheet electrodes could be attributed to the high structure stability, large surface area and nano-sized pores for short path lengths of ion diffusion and electron transport. These results indicated that the mesoporous CuO nanosheet could be a promising candidate to be used as the electrode material of electrochemical capacitor.
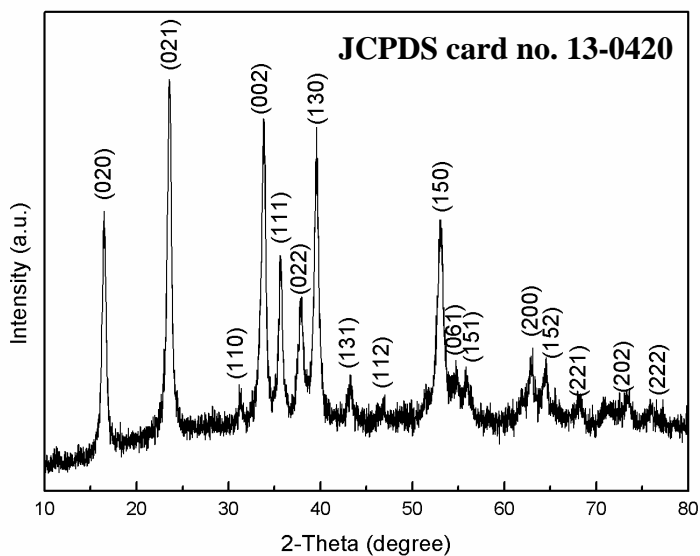
4. CONCLUSIONS

In summary, nanosheet-like, bundle-like and flower-like CuO nanostructures were successfully prepared by a simple wet-chemical method combined with subsequent calcination process. Based on tests of these porous CuO nanostructures as pseudocapacitor electrode materials, it was found that the morphology of the CuO nanostructure can influence the electrochemical properties significantly. The CuO nanosheets exhibited a higher utilization efficiency and better property for electrolyte diffusion than the bundle-like and flower-like nanostructures. The obtained CuO nanosheets electrodes exhibited a moderate specific capacitance and stable cycling performance for supercapacitors. Considering low cost, abundant resources, simplicity of the preparative method and their improved electrochemical properties, CuO nanostructures could be considered as promising electrode materials for electrochemical capacitors.
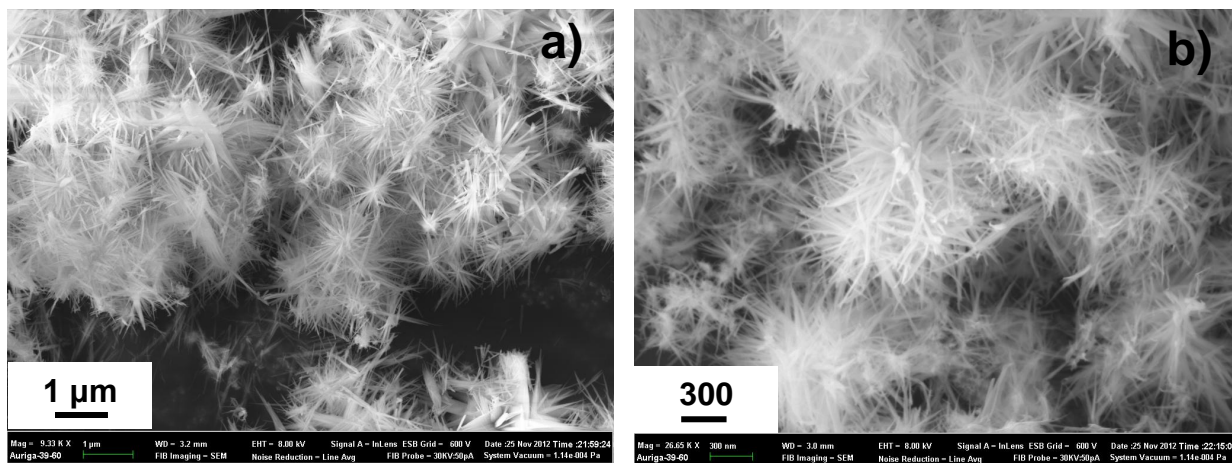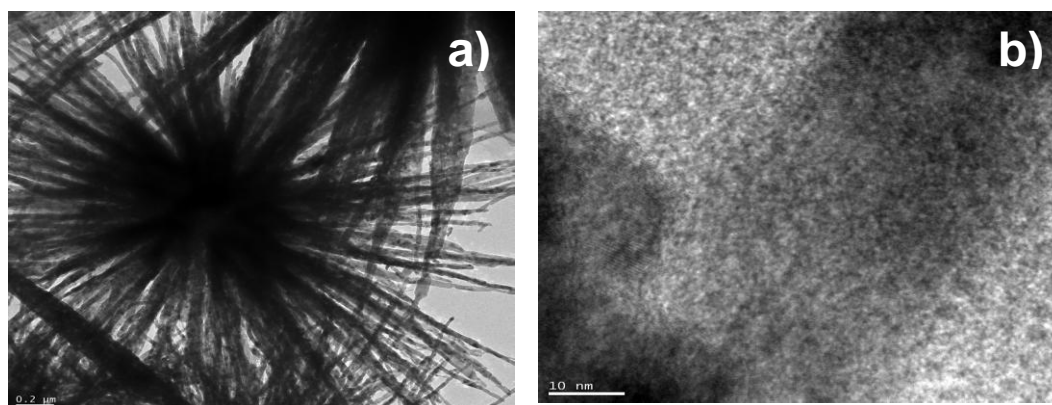
Supplementary information:

SI-1. XRD patterns of $Cu(OH)_2$ precursor nanocrystallines obtained in presence of TOAB and NaOH at room temperature with 6 mL $NH_3 \cdot H_2O$.

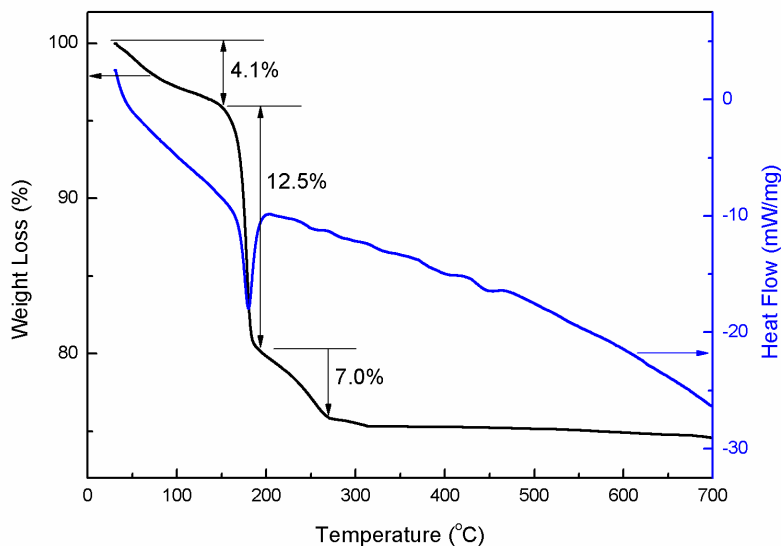**SI-2.** Morphology of $Cu(OH)_2$ precursor nanocrystallines prepared with 6 mL $NH_3 \cdot H_2O$ at room temperature with different magnification.

SI-3. TEM (a) and HRTEM (b) images of the flower-like CuO prepared with 8 mL $NH_3 \cdot H_2O$ in presence of TOAB and NaOH at room temperature with continuous stirring for 1.5 h.

SI-4. TGA-DSC curves of the as-prepared $Cu(OH)_2$ precursor obtained with 2 mL $NH_3 \cdot H_2O$ in presence of TOAB and NaOH at room temperature.

References

1. L. Bao, J. Zang and X. Li, *Nano Lett.*, 11 (2011) 1215.
2. T. Brezesinski, J. Wang, S.H. Tolbert and B. Dunn, *Nat. Mater.*, 9 (2010) 146.
3. Y. Hou, Y. Cheng, T. Hobson and J. Liu, *Nano Lett.*, 10 (2010) 2727.
4. P. Simon and Y. Gogotsi, *Nat. Mater.*, 7 (2008) 845.
5. G. Wang, L. Zhang and J. Zhang, *Chem. Soc. Rev.*, 41 (2012) 797.
6. B.E. Conway, *Electrochemical Supercapacitors: Scientific Fundamentals and Technological Applications,* Kluwer Academic/Plenum Publishers, New York , (1999).
7. L.-Q. Mai, F. Yang, Y.-L. Zhao, X. Xu, L. Xu and Y.-Z. Luo, *Nat. Commun.*, 2 (2011).
8. W. Chen, R.B. Rakhi, L. Hu, X. Xie, Y. Cui and H.N. Alshareef, *Nano Lett.*, 11 (2011) 5165.
9. R.B. Rakhi, W. Chen, D. Cha and H.N. Alshareef, *Nano Lett.*, 12 (2012) 2559.
10. K. Xie, X. Qin, X. Wang, Y. Wang, H. Tao, Q. Wu, L. Yang and Z. Hu, *Adv. Mater.*, 24 (2012) 347.
11. X. He, R. Li, J. Qiu, K. Xie, P. Ling, M. Yu, X. Zhang and M. Zheng, *Carbon*, 50 (2012) 4911.
12. L. Zhang and G. Shi, *J. Phys. Chem. C*, 115 (2011) 17206.
13. Y. Zhang, H. Feng, X. Wu, L. Wang, A. Zhang, T. Xia, H. Dong, X. Li and L. Zhang, *Int. J. Hydrogen Energ.*,34 (2009) 4889.
14. G. Yu, L. Hu, N. Liu, H. Wang, M. Vosgueritchian, Y. Yang, Y. Cui and Z. Bao, *Nano Lett.*, 11 (2011) 4438.
15. L.L. Zhang, S. Li, J. Zhang, P. Guo, J. Zheng and X.S. Zhao, *Chem. Mater.*, 22 (2010) 1195.
16. C.C. Hu and W.C. Chen, *Electrochim. Acta*, 49 (2004) 3469.
17. N. Terasawa, K. Mukai and K. Asaka, *J. Mater. Chem.*, 22 (2012) 15104.
18. Y. Murakami, T. Nakamura, X.G. Zhang and Y. Takasu, *J. Alloys Compd.*, 259 (1997) 196.
19. Z.-S. Wu, D.-W. Wang, W. Ren, J. Zhao, G. Zhou, F. Li and H.-M. Cheng, *Adv. Funct. Mater.*, 20 (2010) 3595.
20. D. Wang, Q. Wang and T. Wang, *Nanotechnology*, 22 (2011).
21. Y.X. Zhang, S.J. Zhu, M. Dong, C.P. Liu and Z.Q. Wen, *Int. J. Electrochem. Sci.*, 8 (2013) 2407.
22. Y. Xiao, Q. Zhang, J. Yan, T. Wei, Z. Fan and F. Wei, *J. Electroanal. Chem.*, 4 (2012) 32.

23. Zhang, X.H. Xia, J.P. Tu, Y.J. Mai, S.J. Shi, X.L. Wang and C.D. Gu, *J. Power Sources*, 199 (2012) 413.
24. D. Han, X. Jing, J. Wang, P. Yang, D. Song and J. Liu, *J. Electroanal. Chemistry*, 682 (2012) 37.
25. L. Xie, K. Li, G. Sun, Z. Hu, C. Lv, J. Wang and C. Zhang, *J. Solid State Electr.*, 17 (2013) 55.
26. G. Sun, K. Li, C. Sun, Y. Liu and H. He, *Electrochim. Acta*, 55 (2010) 2667.
27. V.D. Patake, S.S. Joshi, C.D. Lokhande and O.-S. Joo, *Mater. Chem. Phys.*, 114 (2009) 6.
28. D.P. Dubal, D.S. Dhawale, R.R. Salunkhe, V.S. Jamdade and C.D. Lokhande, *J. Alloys Compd.*, 492 (2010) 26.
29. H. Zhang and M. Zhang, *Mater. Chem. Phys.*,108 (2008) 184.
30. H. Zhang, J. Feng and M. Zhang, *Mater. Res. Bull.*, 43 (2008) 3221.
31. Y. Li, S. Chang, X. Liu, J. Huang, J. Yin, G. Wang and D. Cao, *Electrochim. Acta*, 85 (2012) 393.
32. G. Wang, J. Huang, S. Chen, Y. Gao and D. Cao, *J. Power Sources*, 196 (2011) 5756.
33. R. Sahay, P.S. Kumar, V. Aravindan, J. Sundaramurthy, W.C. Ling, S.G. Mhaisalkar, S. Ramakrishna and S. Madhavi, *J. Phys. Chem. C*, 116 (2012) 18087.
34. C.W. Zou, J. Wang, F. Liang, W. Xie, L.X. Shao and D.J. Fu, *Curr. Appl. Phys.*, 12 (2012) 1349.
35. V. Dhanasekaran, T. Mahalingam, R. Chandramohan, J.-K. Rhee and J.P. Chu, *Thin Solid Films*, 520 (2012) 6608.
36. J. Liu, J. Jin, Z. Deng, S.-Z. Huang, Z.-Y. Hu, L. Wang, C. Wang, L.-H. Chen, Y. Li, G. Van Tendeloo and B.-L. Su, *J. Colloid. Interface Sci.*, 384 (2012) 1.
37. S.C. Vanithakumari, S.L. Shinde and K.K. Nanda, *Mater. Sci. Eng. B-Adv.*, 176 (2011) 669.
38. X. Wang, C. Hui, H. Liu, G. Du, X. He and Y. Xi, *Sensor. Actuat. B-Chem.*, 144 (2010) 220.
39. M. Yang and J. He, *J. Colloid. Interface Sci.*, 355 (2011) 15.
40. C.H. Lu, L.M. Qi, J.H. Yang, D.Y. Zhang, N.Z. Wu and J.M. Ma, *J. Phys. Chem. B*, 108 (2004) 17825.
41. Y.X. Zhang, M. Huang, M. Kuang, C.P. Liu, J.L. Tan, M. Dong, Y. Yuan, X.L. Zhao and Z.Q Wen, *Int. J. Electrochem. Sci.*, 8 (2013) 1366 .
42. M.U.A. Prathap, B. Kaur and R. Srivastava, *J. Colloid. Interface Sci.*, 370 (2012) 144.
43. S.H. Park and H.J. Kim, *J. Am. Chem. Soc.*, 126 (2004) 14368.
44. X. Liu, Z. Li, Q. Zhang, F. Li and T. Kong, *Mater. Lett.*, 72 (2012) 49.
45. J. Xia, H. Li, Z. Luo, H. Shi, K. Wang, H. Shu and Y. Yan, *J. Phys. Chem. Solid*s, 70 (2009) 1461.
46. C. Li, Y. Yin, H. Hou, N. Fan, F. Yuan, Y. Shi and Q. Meng, *Solid State Commun.*, 150 (2010) 585.
47. S.K. Meher and G.R. Rao, *J. Power Sources*, 215 (2012) 317.
48. S.K. Meher and G.R. Rao, *Nanoscale*, 5 (2013) 2089.
49. G.M. Brisard, J.D. Rudnicki, F. McLarnon and E.J. Cairns, *Electrochim. Acta*, 40 (1995) 859.
50. J. Gao, A. Hu, M. Li and D. Mao, *Appl. Surf. Sci.*, 255 (2009) 5943.
51. M.C. Kang and A.A. Gewirth, *J. Phys. Chem. B*, 106 (2002) 12211.
52. M. Jayalakshmi and K. Balasubramanian, *Int. J. Electrochem. Sci.*, 3 (2008) 1277.
53. B. Zhao, P. Liu, H. Zhuang, Z. Jiao, T. Fang, W. Xu, B. Lu and Y. Jiang, *J. Mater. Chem. A*, 1 (2013) 367.
54. Y. Xiao, A. Zhang, S. Liu, J. Zhao, S. Fang, D. Jia and F. Li, *J. Power Sources*, 219 (2012) 140.
55. J. Shao, X. Li, Q. Qu and Y. Wu, *J. Power Sources*, 223 (2013) 56.
56. C. Yuan, X. Zhang, L. Su, B. Gao and L. Shen, *J. Mater. Chem.*, 19 (2009) 5772.
57. X. Zhang, W. Shi, J. Zhu, D.J. Kharistal, W. Zhao, B.S. Lalia, H.H. Hng and Q. Yan, *Acs Nano*, 5 (2011) 2013.